Line defects and quantum Hall plateaus in graphene

V Dal Lago and L E F Foa Torres

Instituto de Física Enrique Gaviola (CONICET) and FaMAF, Universidad Nacional de Córdoba, Argentina

E-mail: lfoa@famaf.unc.edu.ar

CrossMark

Abstract

Line defects in graphene can be either tailored-growth or arise naturally and are at the center of many discussions. Here we study the multiterminal conductance of graphene with an extended line defect in the quantum Hall regime analyzing the effects of the geometry of the setup, disorder and strain on the quantum Hall plateaus. We show that the defect turns out to affect the local and non-local conductance in very different ways depending on the geometrical configuration. When the defect is parallel to the sample edges one gets an equivalent circuit formed by parallel resistors. In contrast, when the defect bridges opposite edges, the Hall conductance may remain unaltered depending on the geometry of the voltage/current probes. The role of disorder, strain and the microscopic details of the defect in our results is also discussed. We show that the defect provides a realization of the electrical analog of an optical *beam splitter*. Its peculiar energy dependent inter-edge transmission allows it to be turned on or off at will and it may be used for routing the chiral edge states.

Keywords: graphene, line-defects, Hall effect

(Some figures may appear in colour only in the online journal)

1. Introduction

Graphene samples exhibit ballistic electronic transport over micrometer scales even at room temperature [1]. But ripples [2], charge puddles [3] and defects [4] may be more common than not depending on the growth method [4–6]. Common defects include vacancies, topological defects and adsorbates [7, 8]. They can occur naturally and/or be elegantly engineered. This is the case of line defects which occur naturally in polycrystalline samples, but that can also be designed either by a suitable choice of substrate [9] or by simultaneous electron irradiation and Joule heating [10].

Graphene's Landau-level structure [11–13] leads to a half integer quantum Hall effect (QHE) [14, 15] as expressed in units of $4e^2/h$. This contrasts with the integer Hall effect measured in the pioneering works on semiconductors [16] and is one of its most celebrated properties. The large cyclotron energies allow for the remarkable observation of the QHE in graphene even at room temperature [17]. The influence of different types of disorder/defects in the quantum Hall regime has been intensively debated over the last years: from impurities or adatoms, to vacancies and random magnetic fields [18, 19]. More recently, extended defects developing along a line have started to trigger much interest [7, 9]. These line defects induce a valley-dependent scattering [20], or form a quantum one-dimensional channel when adding a suitable staggering potential [21]. In the quantum Hall regime, the ubiquitous line defects at the grain boundaries of polycrystalline samples may form a network which short-circuits the Hall chiral edge states, [22] and their role in the observed quantum Hall response is still an important open question [5, 22, 23]. Previous studies indicate that the presence of extended defects almost automatically destroy the *two-terminal* (local) conductance plateaus [22, 24] while a longitudinal resistance develops [23]. However, experiments show that the *non-local* conductance plateaus predicted for pristine graphene remain even in mm-sized
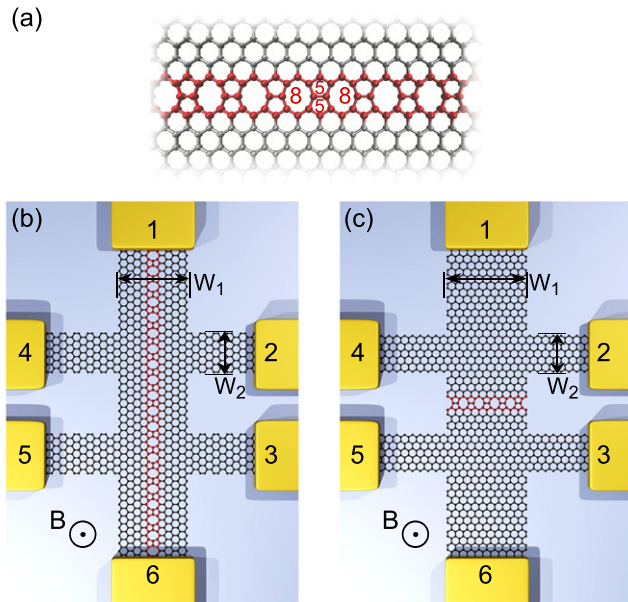
(a)

(b)   (c)

Figure 1. (a) Ball and stick model of the 5-8-5 line defect considered in the text. Multi-terminal setups with the defect *parallel* to the edges (b) and *perpendicular* to the edges (c). A magnetic field is applied perpendicularly to the graphene sheet giving rise to Landau levels. The system size in this scheme is chosen only for illustration.

CVD samples with deviations of up to one per cent of e^2/h [25].

Here we focus on a single line defect (as shown in figure 1(a)) embedded in a graphene ribbon in the quantum Hall regime. We consider two multi-terminal configurations represented in figures 1(b) and (c), hereafter called *parallel* and *perpendicular*, respectively. By using atomistic models we study how the local and non-local conductances are affected by the defect in these two cases as well as the role of disorder and strain. By local conductance we mean the usual two-terminal conductance where the current and voltage are measured in between the same electrodes (as shown in the insets of figures 2(a) and (b)), while the non-local conductance corresponds to the conductance measured in the Hall configuration, where the bias voltage is measured perpendicular to the injected current (see insets of figures 2(c) and (d)). Our results show that the defect sustains roughly localized states which in the presence of the magnetic field behave as boundary states which, depending on the specific energy, may move predominantly in opposite directions on each side of the defect (much like for the case of chiral states). Regarding the transport response, in the *parallel* setup the Hall conductance is that of two resistors in parallel being the sum of the conductance of pristine graphene and a contribution due to states around the defect. In the *perpendicular* case, the defect allows for inter-edge conduction (increasing the longitudinal resistance) but does not necessarily affect the *non-local* conductance plateaus. Indeed, depending on the geometry of the voltage and current probes it may not change it at all, emphasizing the importance of the geometry in the non-local response. Moreover, thanks to the peculiar energy-dependent inter-edge transmission this *beam splitter* can be

turned on or off by applying a gate voltage. Finally, we also discuss the role of disorder, strain and of the microscopic details on our results as well as their possible role in the experimental measurements in large samples.

2. Atomistic model

We use a tight-binding Hamiltonian to describe the electrons near the Fermi energy in graphene [26–28],

$$\mathcal{H} = \sum_i \varepsilon_i\, c_i^\dagger c_i - \sum_{\langle i,j\rangle} [\gamma_{ij}\, c_i^\dagger c_j + \mathrm{h.c.}]\,, \tag{1}$$

where $c_i^\dagger$ and c_i are the electronic creation and annihilation operators at the π-orbital on site i, $\varepsilon_i = 0$ is the on-site energy, and γ_{ij} is the nearest-neighbors hopping matrix element (which is taken here so that $|\gamma_0| = 2.7\,\mathrm{eV}$ in absence of an external perturbation, see [27]).

The magnetic field is described through a Peierls substitution, which modifies the phase of the hopping matrix elements [28, 29]:

$$\gamma_{ij} = \gamma_0 \exp\left(\mathrm{i}\frac{2\pi}{\Phi_0} \int_{r_i}^{r_j} \boldsymbol{A}\cdot\mathrm{d}\boldsymbol{\ell}\right)\,, \tag{2}$$

where Φ_0 is the magnetic flux quantum. For simplicity we consider an 'all graphene' device where the leads are also graphene ribbons extending to infinity. To avoid reflections the magnetic field is applied to the whole device including the leads. The magnetic field is chosen so that the decay length of the edge states towards the sample ξ is much smaller than the sample width W. In this multi-terminal case one needs to smoothly change the gauge so that it preserves the translational invariance on each terminal. To this end we use a Landau gauge following the prescription given in [30].

Within this tight-binding Hamiltonian, the line defect is assumed to change the lattice topology only (shown in figure 1(a)). A more accurate parametrization of the hoppings and on-site energies would give a small variation of the hoppings of less than a few per cent [21] and is disregarded. Magnetic effects deriving from the spin-polarization of the states around the defect are not considered [31, 32], which could add interesting effects on top of the physics described here. The 5-8-5 configuration of figure 1(a) breaks the bipartite nature of the graphene lattice, thus breaking the electron-hole symmetry.

The conductance in the coherent zero-temperature limit follows from the Landauer–Büttiker formalism [33, 34]. Specifically, the current at lead α in the low bias and low-temperature limit is given by:

$$\mathcal{I}_\alpha = \frac{2e}{h} \sum_\beta \left[\mathcal{T}_{\beta,\alpha}(\varepsilon_\mathrm{F})\mu_\alpha - \mathcal{T}_{\alpha,\beta}(\varepsilon_\mathrm{F})\mu_\beta\right], \tag{3}$$

where $\mathcal{T}_{\beta,\alpha}$ is the transmission probability from lead α to β and $\{\mu_\alpha\}$ are the chemical potentials of each lead. Our calculations use an implementation based on Kwant [35] to determine

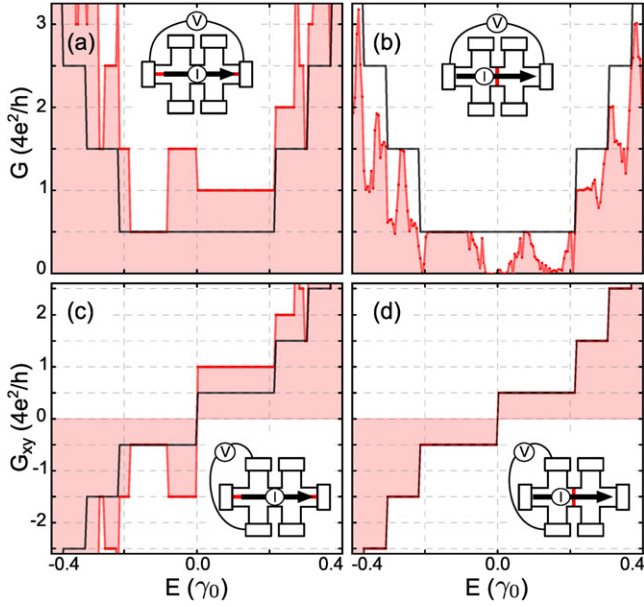**Figure 2.** Two-terminal conductance G for the *parallel* (*a*) and *perpendicular* (*b*) setups as a function of the Fermi energy. The Hall conductance G_{xy} for the same configurations is shown in (*c*) and (*d*). The results for pristine graphene are also shown with a solid black line. The inset on each panel shows the corresponding setup for easier reference. All the cases were calculated for $W_1 = 37.4$ nm and $W_2 = 24.8$ nm. The device is threaded by a magnetic flux of $0.013\Phi_0$ per plaquette.

$\mathcal{T}_{\beta,\alpha}$. With this information, one fixes a small bias voltage $\delta V = (\mu_1 - \mu_6)/e$ between leads 1 and 6 and then solves for the two-terminal conductance $G = \mathcal{I}_1/\delta V$, and for the Hall conductance $G_{xy} = e\mathcal{I}_1/(\mu_2 - \mu_4)$.

3. Multiterminal conductance and edge/boundary states

We start by presenting the local and non-local conductances in figure 2 (red line with shaded area underneath). The top panels (figures 2(*a*) and (*b*)) show the two-terminal conductance and the bottom panels (figures 2(*c*) and (*d*)) show the Hall conductance. The panels on the left (right) show the results for the *parallel* (*perpendicular*) setup. For reference, we also include the results for pristine graphene with a solid black line.

In the case of the *parallel* configuration the conductance G (red with a dashed area underneath) develops new plateaus, a fingerprint of ballistic transport. These plateaus evidence a number of conducting channels which are larger than that of pristine graphene (black line). In contrast, for the *perpendicular* case (figure 2(*b*)) the addition of the line defect strongly deters transport in most of the presented energy range. This occurs roughly in the same regions where transport is enhanced in figure 2(*a*).

The Hall conductance curves complete the above picture. For the *parallel* configuration new plateaus emerge in G_{xy} (figure 2(*c*)), consistent with the ballistic behavior of the *local* conductance. Interestingly, for the *perpendicular* setup where the defect bridges the opposite sample edges, the Hall plateaus of pristine graphene are fully preserved (the red
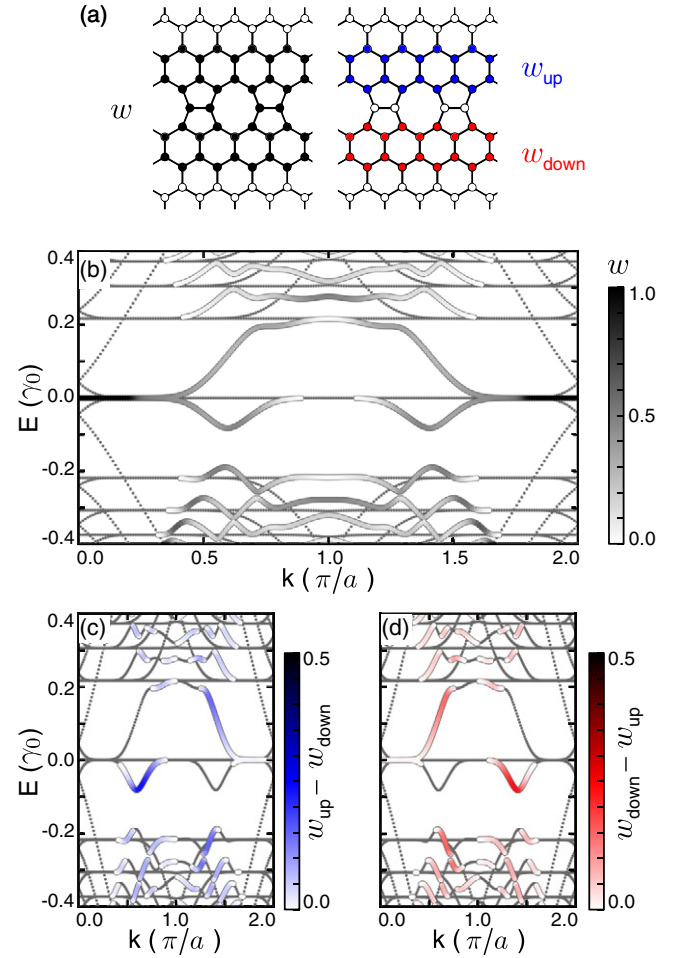

Figure 3. (*a*) Scheme of a 5-8-5 line defect. The atoms used in the calculation of the weight w, w_{up} and w_{down} are marked with full colors. (*b*) The bandstructure for a 5-8-5 line defect embedded at the center of a zigzag ribbon. States having a weight (modulus squared of the probability amplitude) larger than 0.01 on the atoms around the defect are shown on a color scale from white ($w = 0$) to black ($w = 1$). (*c*) Same as (*b*) but this time the color scale corresponds to $w_{up} - w_{down}$ (only positive values are shown), that is, states with a weight predominantly on the upper part of the defect. (*d*) Same as (*b*) but for the partial weight $w_{down} - w_{up}$.

and black curves are on top of each other). The contrast between figures 2(*b*) and (*d*) is evident. How is the mechanism weakening in the same way as the two-terminal conductance but at the same time is able to keep the Hall plateaus unaltered?

Let us now examine the bandstructure of an infinite zigzag ribbon hosting a line defect at its center. This is shown in figure 3(*b*) (grey dots). The filled circles in the same figure show states with a weight w on the area around the defect ($2a$ from the center, the corresponding sites are indicated with black in panel (*a*)-left) with a magnitude encoded on the color scale of the filling: white for vanishing weight and black for maximum weight. In addition to the formation of Landau levels as expected for graphene (grey dots), states localized around the defect are also observed (thick color line), in agreement with the main features reported in previous works [36]. These states are much like the Hall states at the sample edges.

One may then wonder: are these states chiral? We find that they are not strictly chiral in the sense that they have a non-zero weight on both sides of the line defect. Nevertheless, for some energies there is a predominant direction of motion and the physics resembles that of chiral states. This can be appreciated in figures 3(c) and (d), where the states moving predominantly on the upper (lower) region of the defect are shown. The partial weight on opposite sides of the defect is denoted with w_{up} and w_{down}, as indicated in figure 3(a)-right.

A related observation is the presence of gaps in the density of states around the defect (e.g. in-between the $n = 0$ and $n = -1$ Landau levels). These gaps appear because of the hybridization among the chiral edge states on each side of the defect. Indeed, reducing the hopping matrix elements connecting the central line of the defect with the rest of the sample narrows the gap. This hybridization also hinders the chirality of the boundary states, as seen in figures 3(b) and (c). Interested readers may find more details in appendix A. Once the presence of this gap in the LDOS is established, one can anticipate that within this gap transport will not be modified by the defect either in the *parallel* or in the *perpendicular* configurations.

A more accurate parametrization requires non-zero on-site energies around the line defect [37]. The main effect of this correction is to introduce a small shift of the line defect's states around zero energy. This does not change our main conclusions, therefore here we keep the simpler description without those on-site terms.

To gain more insight into the transport behavior let us now turn to the scattering states for different energies and asymptotic boundary conditions. Figures 4(a) and (b) show the scattering states for electrons incident from terminal 1 in the *parallel* configuration (see figure 1(b)). Figure 4(a) corresponds to the case of $E = -0.15\gamma_0$ and figure 4(b) is for $E = +0.1\gamma_0$. It can be noticed that the chirality of the states at the sample edges is reversed. Besides, we see that for $E = +0.1\gamma_0$ new conduction channels open up around the line defect. These new channels turn out to be present in almost all the energy range except for example around $E \sim -0.15\gamma_0$ as mentioned previously.

The picture changes drastically for the *perpendicular* configuration. Figures 4(d) and (e) show the scattering states for electrons injected from the top leads marked with arrows. Figure 4(d) corresponds to the case of $E = -0.15\gamma_0$ and figure 4(e) is for $E = +0.1\gamma_0$. Similar to figure 4(a), in figure 4(d) the defect does not provide substantial scattering. However, once the defect is active, as in figure 4(e), we see that it splits the original beam into two parts: the first following on the same edge and the second using the channel localized around the defect to switch sides (see scheme in figure 4(f)). Thus, the defect in this configuration fulfills the function of a *beam splitter*.

In the following we rationalize the previous observations based on a minimal model and discuss the role of disorder, strain and the atomic structure of the defect in our results.

3.1. Minimal model for the multi-terminal conductances

In the following we present a simple model for the conductance matrix that allows us to rationalize the essence of the results.
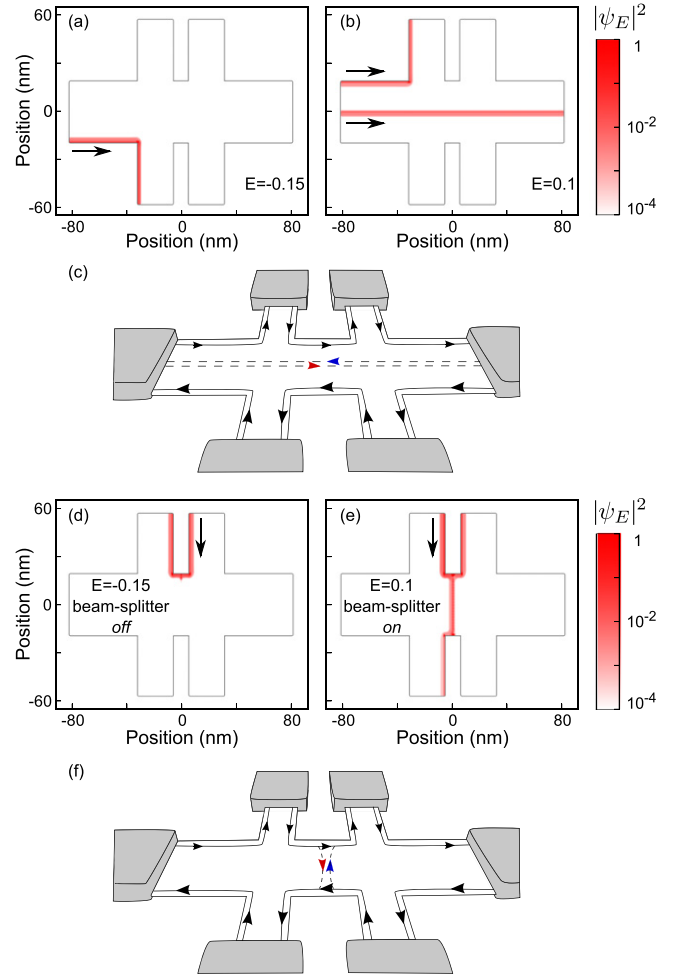

Figure 4. Panels (a), (b), (d) and (e) show the square modulus of the scattering states calculated for an asymptotic condition with electrons incoming from the lead marked with an arrow on each plot. The energy of these states is given in units of γ_0, -0.15 for (a) and (d) and $+0.1$ for (b) and (e). (a) and (b) correspond to the *parallel* setup while (d) and (e) are for the *perpendicular* setup. The schemes in (c) and (f) give a glance at the available edge and boundary states for positive energy. In the *perpendicular* setup (panel (f)), the line defect serves as a *beam splitter*.

This model highlights the importance of the geometrical arrangement and warning on the use of the two-terminal conductance as a proxy for the (non-local) Hall conductance.

Parallel setup. In the low bias, low-temperature limit the currents and voltages follow equation (3) in the main text (see also [33]). A model for the *parallel* setup can be constructed by inspection of the scheme in figure 4(c) in the main text as:

$$\begin{pmatrix} I \\ 0 \\ 0 \\ 0 \\ 0 \\ -I \end{pmatrix} = \begin{pmatrix} \nu_T & 0 & 0 & -\nu_g & 0 & -\nu_d \\ -\nu_g & \nu_g & 0 & 0 & 0 & 0 \\ 0 & -\nu_g & \nu_g & 0 & 0 & 0 \\ 0 & 0 & 0 & \nu_g & -\nu_g & 0 \\ 0 & 0 & 0 & 0 & \nu_g & -\nu_g \\ -\nu_d & 0 & -\nu_g & 0 & 0 & \nu_T \end{pmatrix} \begin{pmatrix} V_1 \\ V_2 \\ V_3 \\ V_4 \\ V_5 \\ V_6 \end{pmatrix}$$

where we have set leads 1 and 6 as the current source and drain, ν_g is the number of edge channels of pristine graphene for the energy under study (the chirality is indicated by the corresponding sign), ν_d is the contribution to the conductance matrix due to the line defect and $\nu_T = \nu_g + \nu_d$. We emphasize that ν_g and ν_d are functions of the carriers energy and the microscopic details of the system.

A simple calculation shows that the inverse resistances follow the sum rule:

$$G_{\text{parallel}} = G_0 + G_{\text{line-defect}}, \qquad (4)$$

$$G_{xy(\text{parallel})} = G_{xy(0)} + G_{xy(\text{line-defect})}, \qquad (5)$$

where the subscript 0 and line-defect indicate, respectively, the conductance for pristine graphene and the contribution due to the channels at the line defect. In this case, G_{xy} is simply given by $G_{xy} = \nu_T/R_0$, where $R_0 = h/(2e^2)$.

Perpendicular setup. A minimal model for this sample maps to that of a 6-terminal Hall configuration with a constriction [34]:

$$\begin{pmatrix} I \\ 0 \\ 0 \\ 0 \\ 0 \\ -I \end{pmatrix} = \begin{pmatrix} \nu_g & 0 & 0 & -\nu_g & 0 & 0 \\ -\nu_g & \nu_g & 0 & 0 & 0 & 0 \\ 0 & -\nu_t & \nu_g & 0 & -\nu' & 0 \\ 0 & -\nu' & 0 & \nu_g & -\nu_t & 0 \\ 0 & 0 & 0 & 0 & \nu_g & -\nu_g \\ 0 & 0 & -\nu_g & 0 & 0 & \nu_g \end{pmatrix} \begin{pmatrix} V_1 \\ V_2 \\ V_3 \\ V_4 \\ V_5 \\ V_6 \end{pmatrix}$$

where ν_g is the number of edge channels of pristine graphene for the energy under study as before, ν' is the fraction that is deflected at the line defect, and $\nu_g = \nu' + \nu_t$. Once more we emphasize that ν' and ν_t depend on the energy of the incoming electrons and the details of the defect. Based on this model one finds $G = (\nu_g - \nu')/R_0$, $G_{xy} = \nu_g/R_0$ and $R_{xx} = \nu'/(\nu_g(\nu_g - \nu')) \times R_0$.

The ratio of the incident electrons whose trajectory is deflected by the line defect, which is given by ν'/ν_g (and it can be seen as the change in the two-terminal conductance in figure 2(b)), has a peculiar energy dependence that allows, for example, for easily switching on or off the *beam splitter* by applying a gate voltage. Figures 4(d) and (e) show a situation where the splitter is off and on respectively. The line defect in this setup can therefore be used as a tool to steer the conduction of the chiral edge states. To predict the precise energy dependence a full atomistic calculation is needed (we refer to the discussion around figure 3).

3.2. Effect of the geometry on the Hall response

Based on the previous discussion we can argue about the dependence of the Hall conductance on the relative position of the defect and voltage probes. Figure 5(a) shows the Hall conductance obtained in a setup where leads 1 and 6 serve as
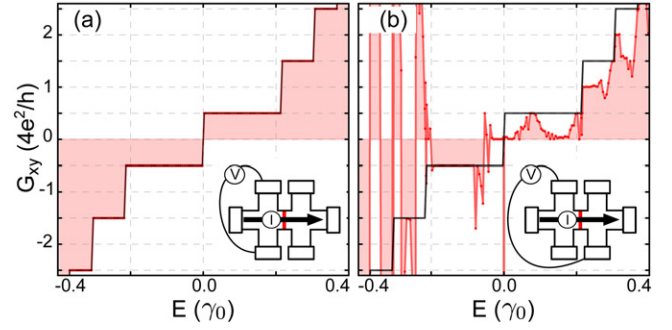

Figure 5. (a) Hall conductance (I:1,6; V:2,4) for the *perpendicular* setup as a function of the Fermi energy (the same as in figure 2(d)). (b) The same as (a) but with the voltage measured between leads 2 and 5, i.e. on opposite sites of the defect. The results for the pristine case are also shown with a solid black line. The inset on each panel shows the corresponding setup for easier reference. All the cases were calculated for $W_1 = 37.4$ nm and $W_2 = 24.8$ nm. The device is threaded by a magnetic flux of $0.013\Phi_0$ per plaquette.

source and drain for the current while the voltage is measured between leads 2 and 4 (same as figure 2(d))[1]. In figure 5(b) the voltage is measured between leads on different sides of the defect (leads 2 and 5), as schematically indicated in the insets. It can be noticed that the first one is independent of the inter-edge transmission and has the same value as for pristine graphene; whereas for the latter, one gets a result resembling the two-terminal conductance.

One can also verify that adding a second defect in the *perpendicular* setup which short-circuits the edge states in lead 1, does not change the Hall response between leads 2 and 4. This can be derived by following a reasoning similar to the one provided in section 3.1.

3.3. Role of the microscopic details in the results

Considering the above analysis it can also be inferred that the defect structure will not affect the main picture reported here, but is crucial in establishing the precise location of the energy-dependent features (plateaus, etc). The minimal model is mainly ruled by: the geometrical arrangement of the leads and the defect, and the microscopic details which are encoded in the energy dependence of the transmission matrix. The peculiarities of graphene enter only through the singular structure of the Hall plateaus (the presence of a Landau level at zero energy and the particular level spacing). The existence of an energy region where the defect states have a gap produced by the hybridization of the states on each side of the defect, as discussed previously, is also quite general.

We verified this in an analogous system with a 5-7-7-5 line defect (see appendix C). Our main conclusions remain valid and only changes in the energy dependence of the conductances are observed. It is interesting to point out that the chirality of the states propagating nearby the defect plays no role in this analysis.

---

[1] Measuring the voltage between leads 3 and 5 gives the same G_{xy}, as shown in figure 5(a).
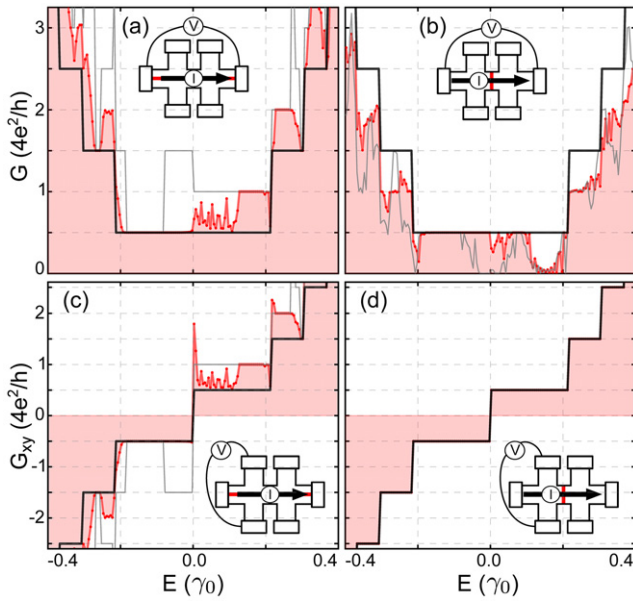
Figure 6. Two-terminal conductance for the *parallel* (*a*) and *perpendicular* (*b*) setups as a function of the Fermi energy. The Hall conductance for the same configurations is shown in (*c*) and (*d*). The red lines with a shaded area underneath are for the system containing a random distribution of long-range impurities, as explained in the main text. The results without disorder are shown for reference with a gray line. The thick black line corresponds to pristine graphene without disorder. All the cases were calculated for $W_1 = 37.4$ nm and $W_2 = 24.8$ nm. The device is threaded by a magnetic flux of $0.013\Phi_0$ per plaquette (same parameters as in figure 2).

3.4. Role of disorder and strain

A natural question concerns the dependence of these results on disorder [22, 24]. We have probed with Anderson disorder, vacancies and long-range impurities. The latter ones were introduced through a modulation of the on-site energies with a gaussian profile as in [28, 38, 39]. Anderson disorder corresponds to the addition of an on-site energy at random on the lattice with a desired concentration (this can be assimilated to the change of a carbon atom with one of other species). The value of this on-site energy is also a random variable, usually taken as uniformly distributed within the range $[-U, U]$ where U measures the disorder strength [28]. In this case, no significant variations were found in the conductance for all the samples when choosing at random on-site energies between $\pm 0.1\gamma_0$ with a concentration of 0.1 per cent.

Figure 6 illustrates the case of four gaussian long-range impurities with $\sigma = 15a$ and intensity $U = \pm 0.2\gamma_0$. These gaussians are centered at most at three σ from the line defect, i.e. where their effect on transport is at a maximum. Additional results for other disorder configurations and for the case of vacancies are included in appendix D. For an arbitrary setup of the voltage probes like the one in figure 5(*b*) we find that it might be quite hard to recover the plateaus in the non-local conductance G_{xy}. Thus, achieving values that are constant within a few percent of e^2/h, as observed in experiments [25], may require high defect densities (of above 0.1 per cent for vacancies). Similar conclusions were reached by other authors examining the two-terminal conductance

using Anderson disorder on either 5-8-5 defects [22] or more complex grain boundaries [24].

Therefore, given the high disorder necessary to recover the plateaus, one may then wonder whether an ingredient other than disorder plays a role in allowing for the recovery of the quantum Hall plateaus. Motivated by this question we explored the effect of mechanical strain localized around the line defect. The results for a strain applied perpendicular to the line defect (following [40]) of about 5 per cent and decaying within a few lattice constants show no important changes in our observations (see appendix B for further details).

4. Conclusions

We study how a single line defect alters the quantum Hall response of a graphene sample. Our results highlight the crucial role played by the geometry, i.e. the relative positions of the defect and voltage/current probes, and the microscopic details of the defect which establishes a peculiar energy dependence of the transport response. Two clearly different situations arise depending on whether the defect is parallel or perpendicular to the samples edges. In the former case, the line defect adds conduction channels fairly localized around it and new plateaus emerge in the *local* and *non-local* conductances. In the latter case, the line defect short-circuits the chiral edge states and its influence on the Hall conductance depends strongly on the placement of the voltage probes. When they are placed on the same side of the line defect, the Hall conductance is the same as in pristine graphene. In contrast, the Hall conductance resembles more closely the two-terminal conductance *only* when the voltage probes are located on opposite sides of the line defect.

In the *perpendicular* setup, the extended defect acts as an electrical analog of a *beam splitter* in optics. Recent experiments show that 5-8-5 line defects can be grown at a predetermined location of a suspended graphene sample [10]. These experiments pave the way for the use of 5-8-5 defects for logical functions and or manipulating the currents flowing along the chiral edge states. Indeed, the results presented here suggest that in the Hall regime they can serve as a *beam splitter* allowing to steer the conduction through the edge states.

Although we considered 5-8-5 and 5-7-7-5 structures for the extended defect, the same physics are expected for other types of boundaries. For the most generic arrangement of voltage probes/defect, our results hint that even with a high density of impurities/disorder it might be hard to recover conductance plateaus in G_{xy} as the ones observed in experiments. Therefore, the role of this building block in more complex geometries, such as those found in poly-crystalline samples, remains an interesting subject for further study.
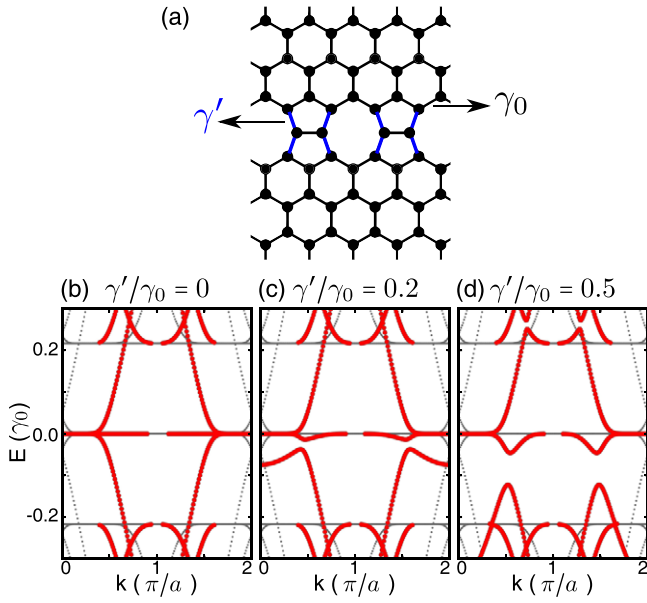
Acknowledgments

Figure 7. (*a*) Scheme of the line defect where the hoppings between the central line with the rest of the sample are denoted by γ'. Turning on this parameter γ' leads to a hybridization of the otherwise chiral edge states, as shown in panels (*b*)–(*d*). States with some degree of localization around the defect are shown in red, others are shown in gray.
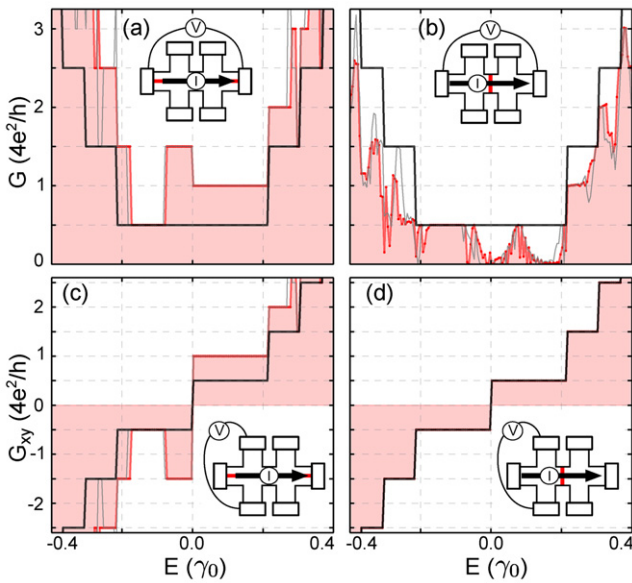

Figure 8. Results for the case of the samples subject to mechanical strain. Two-terminal conductance for the *parallel* (*a*) and *perpendicular* (*b*) setups as a function of the Fermi energy. The Hall conductance for the same configurations is shown in (*c*) and (*d*). The results without strain are shown for reference with a gray line and those for the pristine case with a solid black line. The inset on each panel shows the corresponding setup for easier reference. All the cases were calculated for $W_1 = 37.4$ nm and $W_2 = 24.8$ nm. The device is threaded by a magnetic flux of $0.013\Phi_0$ per plaquette.

Appendix A. Hybridization of the edge states and gaps in the defect's local density of states

The gaps in the local density of states around the defect can be explained considering the model in figure 7(*a*), where the
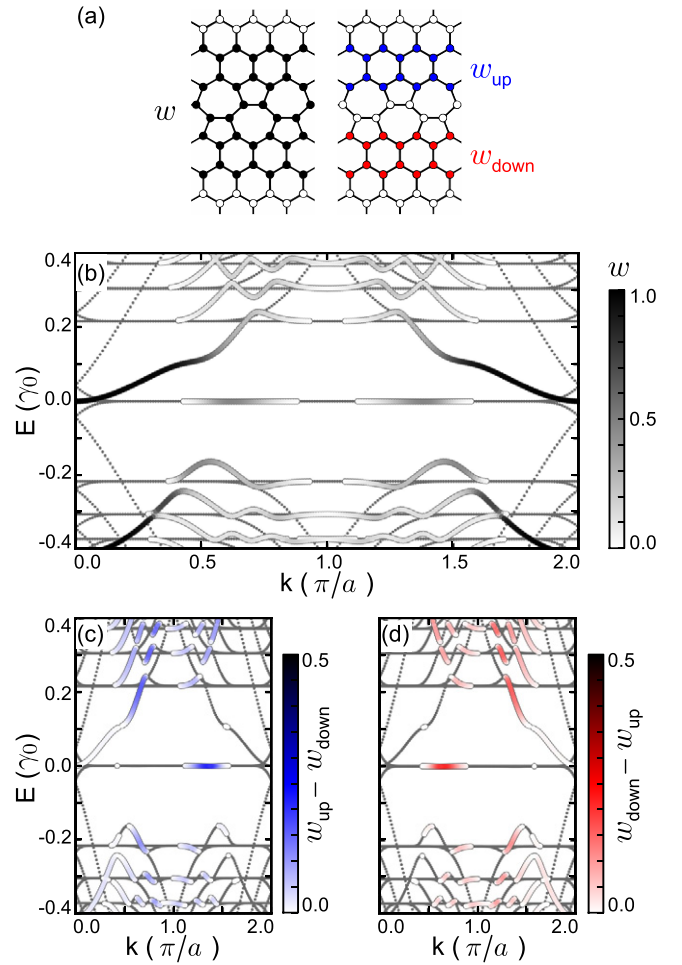

Figure 9. (*a*) Scheme of a 5-7-7-5 line defect. The atoms used in the calculation of the weight w, w_{up} and w_{down} are marked with full colors. (*b*) The bandstructure for a 5-7-7-5 line defect embedded at the center of a zigzag ribbon. States having a weight (modulus squared of the probability amplitude) larger than 0.01 on the atoms around the defect are shown in color scale from white ($w = 0$) to black ($w = 1$). (*c*) Same as (*b*) but this time the color scale corresponds to $w_{up} - w_{down}$ (>0), that is, states with a weight predominantly on the upper part of the defect. (*d*) Same as (*b*) but for the partial weight $w_{down} - w_{up}$.

central part of the defect is connected to the rest of the sample through a hopping γ'. When $\gamma' = 0$ one has two separate samples hosting chiral edge states. As soon as $\gamma' \neq 0$, these chiral edge states become hybridized leading to the gaps observed in the LDOS around the defect. This is illustrated in figures 7(*b*)–(*d*).

Appendix B. Role of strain

We also check the effect in the conductance of the mechanical strain applied locally to the defect region. Figure 8 shows the two-terminal and Hall conductances for a sample subject to a mechanical strain perpendicular to the line defect of 5 per cent and decaying within $3a$ [40]. The results for the case without strain are also shown for a better comparison. No significant changes are seen for both the *parallel* and *perpendicular* setups in comparison to the case without strain.
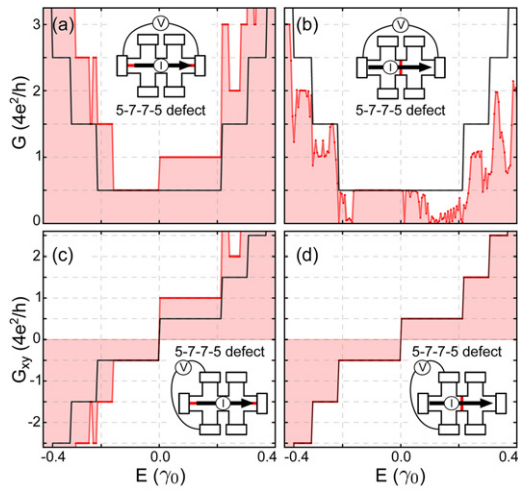
Figure 10. Results for the case of the 5-7-7-5 line defect. Two-terminal conductance for the *parallel* (*a*) and *perpendicular* (*b*) setups as a function of the Fermi energy. The Hall conductance for the same configurations is shown in (*c*) and (*d*). The results for the pristine case are also shown with a solid black line. The inset on each panel shows the corresponding setup for easier reference. All the cases were calculated for $W_1 = 37.4$ nm and $W_2 = 24.8$ nm. The device is threaded by a magnetic flux of $0.013\Phi_0$ per plaquette.

Appendix C. Role of the microscopic structure of the extended defect: the case of a 5-7-7-5 line defect

Based on the analysis given in the main text, one is moved to conclude that the main results reported there do not depend much on the microscopic details of the line defect but rather on the geometry of the setup.

To further support this conclusion we repeated our simulations for a 5-7-7-5 line defect, as represented in figure 9(*a*). Our results for the two-terminal conductance and Hall conductance are shown in figure 10. Figure 9 shows the same spectral information as figure 3 in the main text for the 5-7-7-5 case. Except for the details of the bandstructure which impact on the variations of the two-terminal conductance (figure 10(*a*) and (*b*)), the conclusions achieved in the main text remain valid for this defect. Particularly in the case of the *perpendicular* configuration, the ability to switch on and off the *beam splitter* by changing the gate voltage holds.

Appendix D. Role of disorder

The influence of different types of disorder in our results were further scrutinized. Specifically, we have probed Anderson
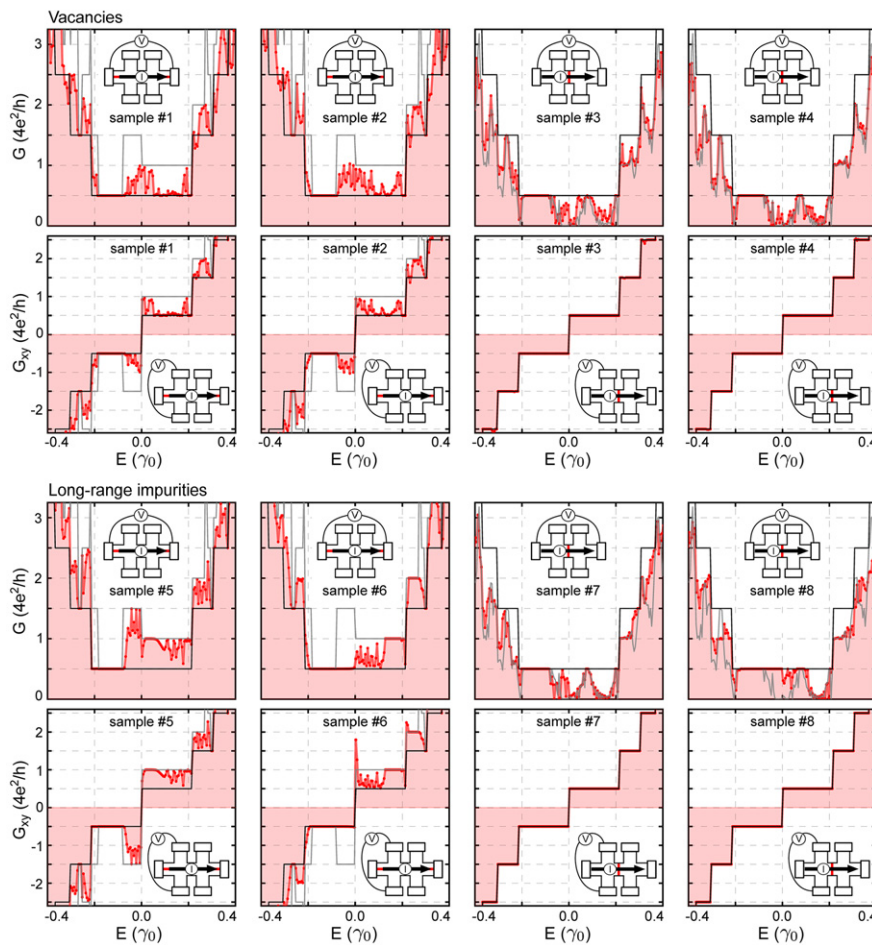

Figure 11. (red line) Two-terminal (*G*) and Hall conductance (G_{xy}) for the *parallel* (samples #1, 2, 5 and 6) and *perpendicular* setups (samples #3, 4, 7 and 8) with vacancies (top) or long-range impurities (bottom) as a function of the Fermi energy. The results without disorder are shown for reference with a gray line and those for the pristine case with a solid black line. The inset on each panel shows the corresponding setup for easier reference. All the cases were calculated for $W_1 = 37.4$ nm and $W_2 = 24.8$ nm. The device is threaded by a magnetic flux of $0.013\Phi_0$ per plaquette.

disorder, vacancies and long-range impurities. The latter ones were introduced through a modulation of the on-site energies with a gaussian profile as in [28, 38, 39]. In the case of the Anderson defects, no significant changes were seen in the conductance for all the samples, when choosing at random on-site energies between $\pm 0.1\gamma_0$. The results for vacancies and long-range impurities are shown in figure 11 for different disorder configurations. Samples 1–4 correspond to vacancies taken at random within the sample with a density of approximately 0.1%. Samples 5–8 are for gaussian impurities localized around the line defect, where the intensity is chosen at random from between $\pm 0.2\gamma_0$ and the decay length was chosen to be $15a$. For the *parallel* setup, 4 gaussians are randomly localized in an area of $350a$ by $120a$ (8σ) around the line defect; whereas in the *perpendicular* case, the area is chosen to be $62a$ by $120a$ (8σ).

These results show that a high density of defects (approximately 0.1% for vacancies and more than 10% for Anderson and long-range disorder) tend to destroy the propagating states along the line defect. As far as the pristine graphene edge states are not demolished, the conductance of pristine graphene is partially recovered.

References

[1] Mayorov A S *et al* 2011 *Nano Lett.* **11** 2396
[2] Fasolino A, Los J H and Katsnelson M I 2007 *Nat. Mater.* **6** 858
[3] Stampfer C, Güttinger J, Hellmüller S, Molitor F, Ensslin K and Ihn T 2009 *Phys. Rev. Lett.* **102** 056403
[4] Terrones M *et al* 2010 *Nano Today* **5** 351
[5] Cummings A W, Duong D L, Nguyen V L, Van Tuan D, Kotakoski J, Barrios Vargas J E, Lee Y H and Roche S 2014 *Adv. Mater.* **26** 5079
[6] Bracamonte M V, Lacconi G I, Urreta S E and Foa Torres L E F 2014 *J. Phys. Chem.* C **118** 15455
[7] Yazyev O V and Louie S G 2010 *Nat. Mater.* **9** 806
[8] Lherbier A, Dubois S M-M, Declerck X, Roche S, Niquet Y-M and Charlier J-C 2011 *Phys. Rev. Lett.* **106** 046803
[9] Lahiri J, Lin Y, Bozkurt P, Oleynik I I and Batzill M 2010 *Nat. Nanotechnol.* **5** 326
[10] Chen J-H, Autes G, Alem N, Gargiulo F, Gautam A, Linck M, Kisielowski C, Yazyev O V, Louie S G and Zettl A 2014 *Phys. Rev. B* **89** 121407
[11] McClure J W 1956 *Phys. Rev.* **104** 666
[12] Castro Neto A H, Guinea F, Peres N M R, Novoselov K S and Geim A K 2009 *Rev. Mod. Phys.* **81** 109
[13] Goerbig M O 2011 *Rev. Mod. Phys.* **83** 1193
[14] Novoselov K S, Geim A K, Morozov S V, Jiang D, Katsnelson M I, Grigorieva I V, Dubonos S V and Firsov A A 2005 *Nature* **438** 197
[15] Zhang Y, Tan Y-W, Stormer H L and Kim P 2005 *Nature* **438** 201
[16] Klitzing K v, Dorda G and Pepper M 1980 *Phys. Rev. Lett.* **45** 494
[17] Novoselov K S, Jiang Z, Zhang Y, Morozov S V, Stormer H L, Zeitler U, Maan J C, Boebinger G S, Kim P and Geim A K 2007 *Science* **315** 1379
[18] Ostrovsky P M, Gornyi I V and Mirlin A D 2008 *Phys. Rev. B* **77** 195430
[19] Ortmann F and Roche S 2013 *Phys. Rev. Lett.* **110** 086602
[20] Gunlycke D and White C T 2011 *Phys. Rev. Lett.* **106** 136806
[21] Song J, Liu H, Jiang H, Sun Q-f and Xie X C 2012 *Phys. Rev.* B **86** 085437
[22] Lafont F *et al* 2014 *Phys. Rev.* B **90** 115422
[23] Cummings A W, Cresti A and Roche S 2014 *Phys. Rev.* B **90** 161401
[24] Bergvall A, Carlsson J M and Lofwander T 2014 arXiv:1408.0394
[25] Shen T, Wu W, Yu Q, Richter C A, Elmquist R, Newell D and Chen Y P 2011 *Appl. Phys. Lett.* **99** 232110
[26] Saito R, Dresselhaus G and Dresselhaus M 1998 *Physical Properties of Carbon Nanotubes* (London: Imperial College Press)
[27] Dubois S M-M, Zanolli Z, Declerck X and Charlier J-C 2009 *Eur. Phys. J.* B **72** 1
[28] Foa Torres L E F, Roche S and Charlier J C 2014 *Introduction to Graphene-Based Nanomaterials: from Electronic Structure to Quantum Transport* (Cambridge: Cambridge University Press)
[29] Lado J L, Gonzalez J W and Fernandez-Rossier J 2013 *Phys. Rev.* B **88** 035448
[30] Baranger H U and Stone A D 1989 *Phys. Rev.* B **40** 8169
[31] Yazyev O V 2010 *Rep. Prog. Phys.* **73** 056501
[32] Botello-Mendez A R, Declerck X, Terrones M, Terrones H and Charlier J-C 2011 *Nanoscale* **3** 2868
[33] Büttiker M 1986 *Phys. Rev. Lett.* **57** 1761
[34] Datta S 1995 *Electronic Transport in Mesoscopic Systems* (Cambridge: Cambridge University Press)
[35] Groth C W, Wimmer M, Akhmerov A R and Waintal X 2014 *New J. Phys.* **16** 063065
[36] Yao H-B, L X-L and Zheng Y-S 2013 *Phys. Rev.* B **88** 235419
[37] R M Guzmán-Arellano and G Usaj private communication
[38] Wakabayashi K, Takane Y and Sigrist M 2007 *Phys. Rev. Lett.* **99** 036601
[39] Ortmann F, Cresti A, Montambaux G and Roche S 2011 *Europhys. Lett.* **94** 47006
[40] Ribeiro R M, Pereira V M, Peres N M R, Briddon P R and Neto A H C 2009 *New J. Phys.* **11** 115002